Chemical Science

Accepted Manuscript

This article can be cited before page numbers have been issued, to do this please use: Y. Gu, Y. Gu, M. Yang, S. Tang, J. Chen, X. Liang, D. Zheng, Z. Li, F. Song, Y. Gao, Y. Zhu, Y. Shi and J. Ma, *Chem. Sci.*, 2025, DOI: 10.1039/D5SC04386G.




ROYAL SOCIETY OF CHEMISTRY

rsc.li/chemical-science

View Article Online
DOI: 10.1039/D5SC04386G

ARTICLE

# High-throughput design of bimetallic materials via the multimodal machine learning and accessibility index

Received 00th January 20xx,
Accepted 00th January 20xx

DOI: 10.1039/x0xx00000x

Yuming Gu [a, ‡], Yating Gu [a, ‡], Maochen Yang [b, ‡], Shisi Tang [a, ‡], Jiawei Chen [a], Xinyi Liang [a], Dong Zheng [c], Zekun Li [b], Fengqi Song [c], Yang Gao [b], Yan Zhu [a, *], Yinghuan Shi [b, *], Jing Ma [a, *]

There is a great challenge for efficient exploration of bimetallic systems containing miscible or even immiscible elements (e.g., Au/Ni, Au/Rh) due to the difficulty in screening candidates with favorable formation energy ($E_{form}$) from the vast combination space of different metal pairs and ligands or coordination environments. The importance of the coordination environment is highlighted through the multilevel attention mechanism within the graph convolutional neural network (GCNN) and the Shapley additive explanation (SHAP) analysis for 8-feature scheme in $E_{form}$ prediction. To further reduce the prediction error of formation energy in test set, the multimodal machine learning (MML) is applied to 11,186 bimetallic nanocluster data by integrating the molecule graph of the metal core and the physical property features such as mixing enthalpy ($H_{mix}$) of the bimetallic pair and SMLES strings and solubility (log*P*) of ligand. The present MML model could predict nanoclusters with up to more than one thousand atoms rapidly. To evaluate the experimental accessibility of bimetallic porous materials, alloys, and 2D materials in a general way, an accessibility index, $\varphi$, is defined as the combination of the electronegativity ($\chi_{env}$) and the reduced atomic distance index ($\tilde{D}$) without the need of density functional theory (DFT) calculations. Larger values of $\varphi$ indicate that the bimetallic materials are more accessible, owing to the energetically favorable interatomic charge tranfer and optimal reduced distance around 0.3 (~3.5 Å metal-metal distance) for nanoclusters and 0.1 (~2.5 Å) for zeolites, respectively. Among the 100 external test samples, three nanoclusters ($Au_{36}Ag_{38}((CF_3)_2PhC{\equiv}C)_{30}Cl_{10}$, $Au_{38}Ag_{33}((CF_3)_2PhC{\equiv}C)_{30}Cl_8$, and $Au_9AgRh(PPh_3)_8Cl$) and three 2D materials (Au/Ni@NC, Ni/Pt@NC, and Cu/Gd@NC) were synthesized in this work, in good agreement with that their accessibility indices ($\varphi$) are in the favorable range ($\varphi$ > -0.30) and low formation energies below -1 eV/atom. The proposed MML scheme and accessibility index hold promise in facilitating the high-throughput discovery and bimetallic material design.

## Introduction

The combination of two different kinds of metal elements brings unique adsorption and luminescence properties in various functional bimetallic systems such as ligand-protected nanoclusters, nanoparticles, alloys, and two-dimensional (2D) materials with potential applications in catalysis, sensors, and drug delivery. [1-6] It is interesting to study the accessibility of bimetallic materials with miscible or even immiscible metal pairs, whose miscibility is reflected by the heat of mixing ($H_{mix}$) in binary phase diagrams that for solid solutions $H_{mix}$ < 0 and phase-separated systems $H_{mix}$ > 0. The mixing of immiscible elements like Ag/Ni, Ag/Cu, Au/Rh, Au–Pt, *etc.*, has been realized in nanomaterials via various methods such as nonequilibrium synthesis[3], colloidal co-reduction [7-10], physical co-sputtering [11], quenching [12-13], or size reduction methods [14]. For the nanoclusters, which are composed of a certain number of metal atoms and ligands, some heteroatom-doped gold nanoclusters with miscible (Au/Cd, Au/Cu) [15-16] and immiscible (Au/Ru, Au/Rh, Au/Pt) elements [17-18] have aroused experimental and theoretical interest. When exploring novel bimetallic systems with miscible or immiscible pairs, there exists several challenges. The vast compositional and structural space, involving diverse element types, stoichiometries, and coordination motifs, exceeds the manual exploration. Screening suitable formation energies ($E_{form}$) among numerous possible metal-ligand combinations is particularly challenging. The strong influence of coordination environments further increases the complexity of stability prediction. Density functional theory (DFT) calculations for large-sized systems are computationally expensive, while experimental synthesis of such bimetallic systems often involves high uncertainty and cost. A predictive machine learning (ML) framework to effectively evaluate the thermodynamic stability and accessibility of the bimetallic materials is desired to save the computational and experimental costs.

Recent advances in ML have enabled stability prediction for materials using diverse data modalities. For instance, the graph

[a] State Key Laboratory of Coordination Chemistry, School of Chemistry and Chemical Engineering, Nanjing University, Nanjing, 210023, P. R. China
[b] State Key Laboratory for Novel Software Technology, Nanjing University, Nanjing, 210023, P. R. China
[c] National Laboratory of Solid State Microstructures, Collaborative Innovation Center of Advanced Microstructures, and School of Physics, Nanjing University, Nanjing 210093, P. R. China; Atom Manufacturing Institute (AMI), Nanjing 211805, P. R. China

†Electronic Supplementary Information (ESI) available. See DOI:10.1039/x0xx00000x

‡ Y. Gu, Y. Gu, M. Yang and S. Tang contributed equally to this work.

DOI: 10.1039/D5SC04386G

modality was applied to give the prediction of the formation energies of the Au nanoclusters, guiding the experimental synthesis of new structures ($Au_{10}(PPh_3)_7Cl_3$ and $Au_{38}OT_{24}$). [19] A quantitative metric of synthesizability for inorganic materials denoted as the crystal-likeness score (CLscore) was predicted by the graph modality via positive-unlabeled learning. [20] In the context of bimetallic nanoclusters, several numeric descriptors, including cohesive energy differences, atomic radius mismatch ($\Delta R$), coordination asymmetry, and magnetism have been employed to build the relationship between the core–shell preference of the bimetallic nanoclusters. [21] Despite of these progresses, relying solely on a single modality alone is insufficient for machine learning models to accurately predict target properties in some cases. Recently, multimodal machine learning (MML) integrates heterogeneous data streams, such as graph and text within a shared latent space, was applied to enhance the efficiency of energy predictions for adsorption configurations to accelerate the catalyst design. [22] MML was also applied to investigate the key role of chemical structure in governing per- and polyfluoroalkyl substances removal, which visualized the contributions of individual chemical elements via adding the simplified molecular input line entry system (SMILES) strings modality into the numeric modality of the experimental data. [23] In addition, by fusing informatics from the modalities of chemical composition (text) and crystal structures (graph), several novel materials, such as $Li_{1.5}NbO_{0.5}F_{0.5}$, $Li_{15}TaN_7O_2$, were recommended as promising candidates for Li-ion conductors. [24]

In this study, we develop an MML model to predict the formation energies of bimetallic nanoclusters with up to thousands of atoms quickly from 11,186 configurations of bimetallic nanoclusters by DFT calculations, as shown in **Fig. 1**. The MML model integrates the informatics from three modalities: (1) graph-based representations of core motifs, (2) SMILES strings encoding ligands, and (3) digital descriptors capturing key thermodynamic and environmental features. An easily available accessibility index, $\varphi$, was further introduced to quantify the synthetic accessibility of bimetallic materials, which integrates the environment electronegativity ($\chi_{env}$) and the reduced metal-metal distance index ($\tilde{D}$) without the need of DFT calculations. This descriptor shows good transferability to evaluate 100 bimetallic materials reported in literatures, including porous materials, alloys, and 2D materials. By taking $\varphi$ and $E_{form}$ into consideration together, three nanoclusters ($Au_{36}Ag_{38}((CF_3)_2PhC{\equiv}C)_{30}Cl_{10}$, $Au_{38}Ag_{33}((CF_3)_2PhC{\equiv}C)_{30}Cl_8$, and $Au_9AgRh(PPh_3)_8Cl$) and three 2D materials (Au/Ni@NC, Ni/Pt@NC, and Cu/Gd@NC) were synthesized successfully. The proposed multimodal machine learning scheme is expected to accelerate the experimental discovery and synthesis of bimetallic systems from a huge chemical space.

View Article Online
DOI: 10.1039/D5SC04386G



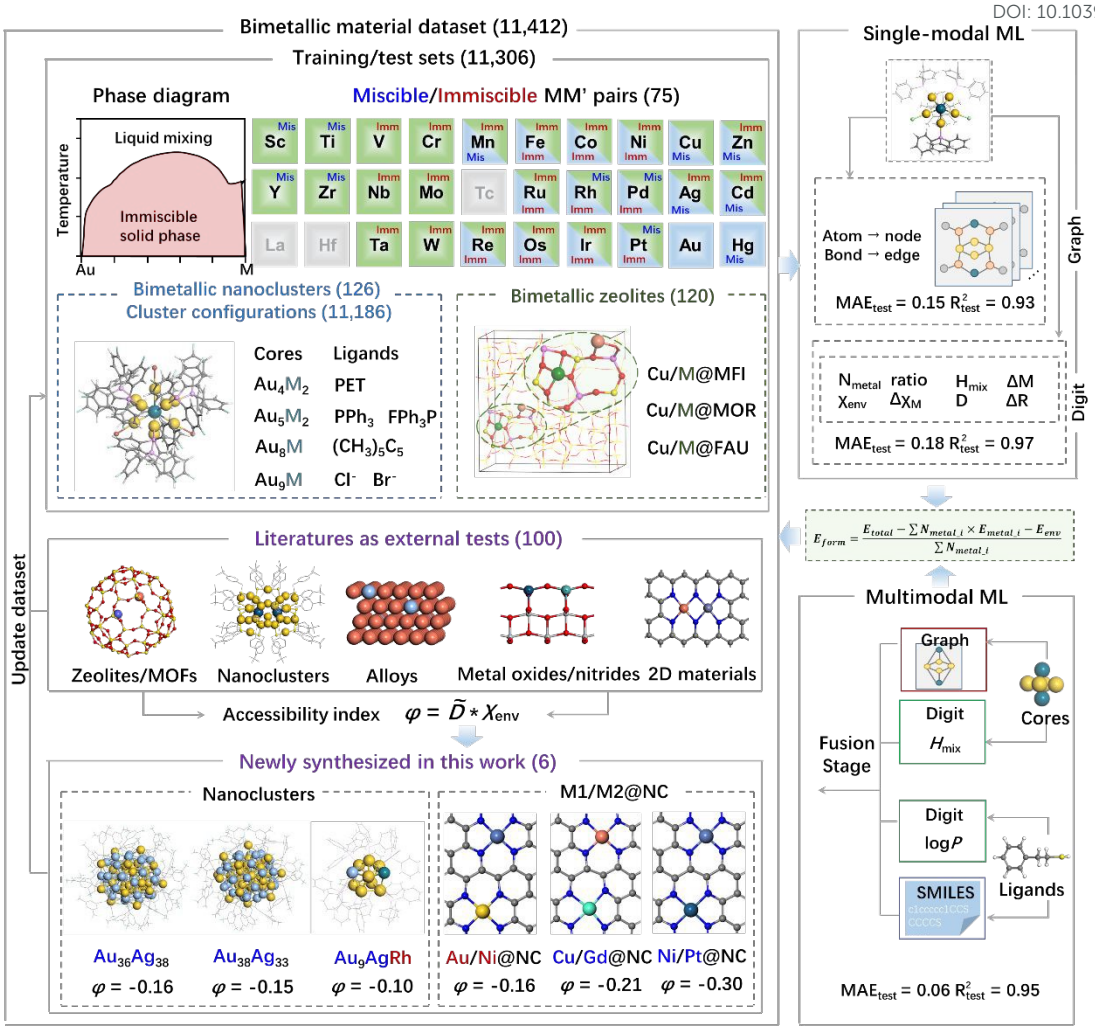


**Fig. 1** The flow chart of the stability and accessibility index prediction of bimetallic materials using multimodal *v.s.* single-modal machine learning methods.

## Results and discussion

### Construction of bimetallic material datasets

Several datasets comprising various nanoclusters have also been developed to facilitate the prediction of stability, bioactivities, and nanohydrophobicity of nanoparticles.[25-27] Here, we focused on the bimetallic combinations in material design. As shown in **Fig. 1**, a dataset of bimetallic materials was compiled with a total of 11,412 unique structures, which spans 75 representative bimetallic element pairs (covering 44 miscible and 31 immiscible combinations). Among them, 11,186 nanocluster configurations sampled from the potential surfaces of 126 nanoclusters and 120 zeolites, were utilized for training and internal testing. To evaluate model generalizability, an external test set consisting of 100 experimentally reported bimetallic materials, including 14 ligand-protected nanoclusters, 4 zeolites/metal-organic frameworks (MOFs), 35 alloys or nanoparticles, 5 oxide/nitride-supported metal systems, and 42 kinds of 2D materials was curated. Six newly synthesized bimetallic structures in this work were also incorporated to update the dataset.

Specifically, bimetallic nanocluster training set is mainly based on 5 types of topology categories, including $Au_4M_2(PET)_8$, $Au_4M_2(PET)_8(PPh_3)_2$, $Au_5M_2((CH_3)_5C_5)_2$ $(PPh_3)_3Cl_2$, $Au_8M(PPh_3)_8$, and $Au_9M(FPh_3P)_7Br_3$ (PET = 2-phenylethanethiol, $PPh_3$ = triphenylphosphine, $FPh_3P$ = tri(4-uorophenyl)phosphine, $(CH_3)_5C_5$ = 1,2,3,4,5-pentamethylcyclopentadienyl). The diversity of bimetallic nanocluster was achieved by the doping heteroatoms into the gold nanoclusters, including Mn, Fe, Co, Ni, Cu, Zn, Ru, Rh, Pd, Ag, Cd, Re, Os, Ir, Pt, and Hg, which generated 126 types of nanoclusters. The configurational flexibility of the ligand also makes the configuration space complicated, since different ligand orientations and binding modes can lead to multiple stable or metastable structures. As a result, we may need to search for the possible structures of nanoclusters. For instance, $Au_4Ru_2(PET)_8$, which contains an $Au_4Ru_2$ core and PET ligands, has been found to have 95 distinct structures due to the flexibility of the ligands and the fluidity of the core structure via the distance between Au and S atoms ($d_{Au-S}$) and the rotation of C-S bond. To systematically capture this

structural diversity, we sampled nanocluster geometries from the potential energy surfaces of 126 nanocluster prototypes with different metal pairs and ligand types, covering both miscible and immiscible combinations. For each nanocluster prototype, multiple configurations were generated by varying the arrangement of metal atoms and the coordination of ligands, followed by DFT calculations to obtain their formation energies. In this way, 11,186 nanocluster configurations were compiled into the present bimetallic dataset, which encompasses a wide range of stoichiometries, coordination environments, and ligands. This dataset was then divided into training, validation, and test sets (8:1:1 ratio) to construct and evaluate the multimodal machine learning (MML) model in the following section.

Metal atoms can also be anchored within the channels in zeolites through coordination interactions with oxygen atoms, forming the metal-zeolites. The distance between two metal atoms (*D*) can be adjusted by the adjacent rings. These bimetallic zeolites are derived from Cu@zeolites with different topologies and pore sizes (PLD), such as MFI (PLD = 6.36 Å), MOR (PLD = 6.70 Å), and FAU (PLD = 11.24 Å). The dopped metals in bimetallic zeolites are mainly 3*d* ~ 5*d* transition metal elements, *i.e.*, Fe/Cu@MFI, shown in **Fig. 1**.

The 100 external test set data were collected from the published literatures, which were synthesized in experiment, including porous materials [28], 2D materials [29-31], metal-loaded metal oxides/nitrides [32-34], alloys [35-36], and nanoclusters [37]. Three newly reported nanoclusters, $Au_{36}Ag_{38}((CF_3)_2PhC{\equiv}C)_{30}Cl_{10}$, $Au_{38}Ag_{33}((CF_3)_2PhC{\equiv}C)_{30}Cl_8$, and $Au_9AgRh(PPh_3)_8Cl$, were added into the external test set. Additionally, three bimetallic pairs supported on nitrogen-doped carbon (NC), namely, Au/Ni@NC, Ni/Pt@NC, and Cu/Gd@NC were newly synthesized in this work, which were also incorporated into the dataset to test the predictive capabilities of the constructed models. The prediction of accessibility was based on two target properties: formation energy ($E_{form}$) and accessibility index ($\varphi$), both of which are defined in detail in the following sections.

**Formation energy prediction: single-modal *v.s.* multimodal machine learning**

To qualitatively evaluate the thermodynamic stability of the bimetallic materials, the formation energy ($E_{form}$) was calculated with the definition shown as follows.

$$E_{form} = \frac{E_{total} - \sum N_{metal_i} \times E_{metal_i} - E_{env}}{\sum N_{metal_i}} (1)$$

In Eq (1), $E_{total}$ was the total energy of the bimetallic nanocluster or zeolite. $N_{metal\_i}$ was the number of the one kind of metal atoms in the bimetallic materials, and $E_{metal\_i}$ was the energy of metal atom, respectively, in which $i$ = 1, 2. $E_{env}$ was the energy of the surrounding environment, for example, ligands for nanocluster, and framework for metal-zeolite. When the formation energy is calculated to be negative, it implies that the bimetallic materials are thermodynamically favorable for experimental synthesis under the given conditions. The computational details were shown in Supporting Information. The formation energy values are mainly populated in the range between -5.86 and 0.85 eV/atom for the bimetallic nanoclusters and zeolites. As shown from the distribution of bimetallic formation energies in dataset in **Fig. S1**, most of the formation energies of bimetallic materials are in the range of -4 ~ -1 eV/atom. A DWeibull-like distribution of $E_{form}$ occurs with $D$ statistic and $p$-value of 0.04 and 0.71 by the Kolmogorov-Smirnov (KS) test, respectively. Two peaks may be ascribed to bimetallic nanoclusters and zeolites data, respectively, in **Fig. S1a** and **S1b**. All structures of the bimetallic nanoclusters were collected into Bimetallic Materials Dataset to train the multimodal machine learning model (**Fig. S2**).

***Formation energy prediction based on GCNN model with graph modality.*** Before exploring multimodal approaches, it is useful to first compare several commonly used single modalities, such as graphs and digital descriptors, which can be applied to predict the formation energy of bimetallic materials. When only the graph modality was applied to represent the bimetallic nanoclusters in graph convolutional neural network (GCNN) model through the home-made DeepMoleNet. [38-39], the input molecular information of the Au nanocluster could be represented by node (atom) and edge (atom pair) automatically, as shown in **Fig. 2**. In this work, the prediction ability was tested by statistic values of mean absolute error (MAE), root mean squared error (RMSE), and coefficient of determination ($R^2$), which are defined as

$$\mathrm{MAE} = \frac{1}{n}\sum_{i=1}^{n} |y_i - \hat{y}_i| (2)$$

$$\mathrm{RMSE} = \sqrt{\frac{1}{n}\sum_{i=1}^{n} (y_i - \hat{y}_i)^2} (3)$$

$$R^2 = 1 - \frac{\sum_{i=1}^{n} (\hat{y}_i - y_i)^2}{\sum_{i=1}^{n} (y_{\bar{i}} - y_i)^2} (4)$$

where $\boldsymbol{y_i}$ are the machine learning predicted results, $\boldsymbol{\hat{y}_i}$ are the actual DFT calculation values, and $\boldsymbol{y_{\bar{i}}}$ are the averaged DFT values, respectively. The GCNN model gives the prediction (MAE = 0.15 eV/atom, $R^2$ = 0.93) for the formation energies of bimetallic nanoclusters, in which hyper-parameters of GCNN are listed in **Table S1**. Four different learning rates were tested to obtain the optimal GCNN model, as shown in **Fig. S3**.

View Article Online
DOI: 10.1039/D5SC04386G

**Table 1.** Coefficient of determination ($R^2$) and mean absolute error (MAE) of ML models with different modalities

| Algorithms | $R^2$ | | MAE | |
|---|---|---|---|---|
| | training set | test set | training set | test set |
| GCNN with graph modality<br>11,186 data (training: validation: test = 8: 1: 1) | | | | |
| GCNN | 0.934 | 0.927 | 0.121 | 0.152 |
| 8-feature scheme ($\chi_{env}$, $\Delta\chi_M$, $N_{metal}$, *ratio*, $\Delta M$, $H_{mix}$, $D$, $\Delta R$)<br>246 data (training: validation: test = 8: 1: 1) | | | | |
| RFR | 0.996 | 0.969 | 0.072 | 0.182 |
| GDB | 0.995 | 0.967 | 0.077 | 0.186 |
| CATBoost | 0.999 | 0.967 | 0.016 | 0.184 |
| DT | 0.993 | 0.966 | 0.093 | 0.198 |
| EXTREE | 0.999 | 0.959 | 0.001 | 0.203 |
| XGB | 0.997 | 0.959 | 0.067 | 0.215 |
| ADAB | 0.955 | 0.909 | 0.261 | 0.325 |
| SVR | 0.979 | 0.855 | 0.100 | 0.375 |
| KNN | 0.934 | 0.810 | 0.261 | 0.324 |
| RIDGE | 0.699 | 0.654 | 0.680 | 0.616 |
| LINEAR | 0.699 | 0.653 | 0.679 | 0.614 |
| LASSO | 0.686 | 0.640 | 0.700 | 0.649 |
| MML (graph+SMILES strings+$H_{mix}$&log$P$)<br>11,186 data (training: validation: test = 8: 1: 1) | | | | |
| MML w/o $H_{mix}$&log$P$ | 0.943 | 0.933 | 0.070 | 0.073 |
| MML with $H_{mix}$ | 0.938 | 0.951 | 0.061 | 0.057 |
| MML with log$P$ | 0.952 | 0.950 | 0.058 | 0.072 |
| MML with $H_{mix}$&log$P$ | 0.963 | 0.952 | 0.050 | 0.055 |

The significance of the coordination environment in stability prediction could be revealed through the multilevel attention mechanism. Local attention operations are performed at T steps following each aggregation of distinct node feature levels. The influence of adjacent atom environments on atomic attention results in shifts in importance at each step. High weight values highlight the crucial roles of specific atoms in the energy prediction process. As shown in **Fig. 2**, taking $Au_4Pd_2(PET)_8$ as an example, the normalized attention values, *Att*, on metal atoms are the highest in the bimetallic nanoclusters, indicating that metal core plays important roles in the $E_{form}$ prediction. The ligands of $PPh_3$, PET, and $(CH_3)_5C_5$ are the top three ligands in the occurrence count, with the log$P$ values of 5.69, 2.87, and 0.40, respectively. It is reported that the log$P$ of the ligand has great influence on the solubility of Au clusters and cell activity. [19] The coordination atoms, *i.e.*, sulfur, also show the relatively high values ($Att_S$ = 0.50). When the $PPh_3$ ligands are added to form $Au_4Pd_2(PET)_8(PPh_3)_3$, the bimetallic nanocluster becomes more stable ($E_{form}$ = -3.63 eV/atom) with the $Att_P$ value of 0.42. It is found that the attention values of C atoms in coordinated $(CH_3)_5C_5$ ($Att_C$ = 0.51) are higher than those in $PPh_3$ ($Att_C$ = 0.1 ~ 0.2) for $Au_5Pd_2((CH_3)_5C_5)_2(PPh_3)_3Cl_2$ nanocluster. Interestingly, the average attention values of ligands ($Att_{ligand}$) exhibit the correlation between the extent of charge transfer between two metals ($\Delta Q_{CT}$). It has been revealed that large extent of charge difference ($\Delta Q_{CT}$) between two metal atoms may lead to a more stable structure. [19] To sum up, the coordination environment, charge transfer, and log$P$ feature of ligand are modulation factors in the stabilization of metal cores. In the following subsection, these features will be used as descriptors in building $E_{form}$ prediction models.

View Article Online
DOI: 10.1039/D5SC04386G



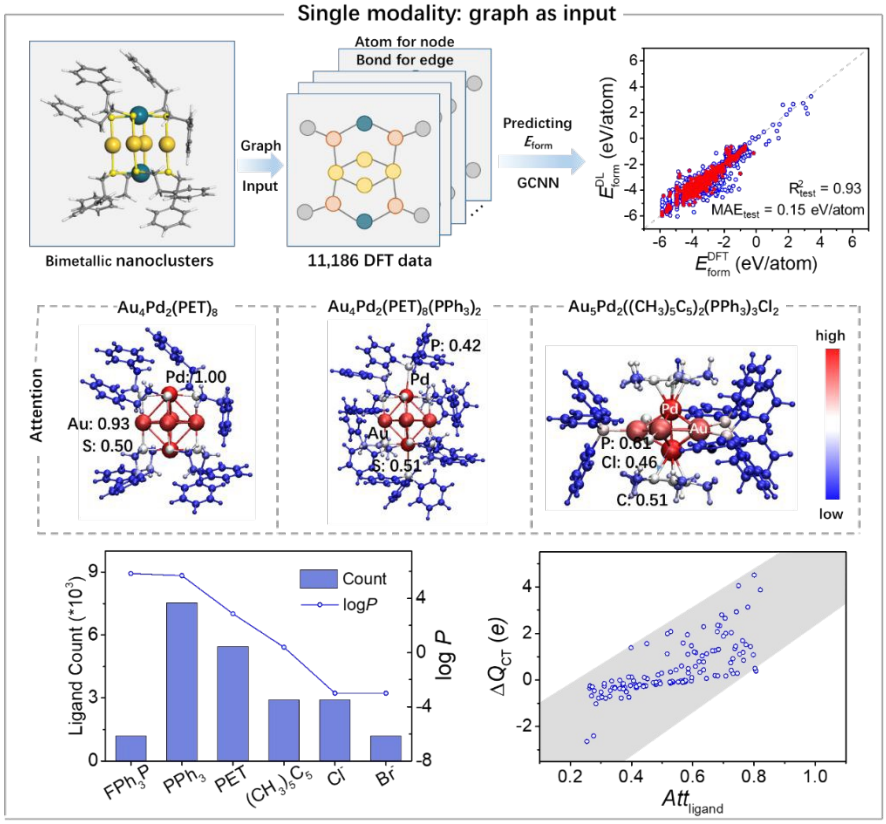


**Fig. 2** The GCNN model based on graph modality for the formation energy prediction.

***Formation energy prediction based on 8-feature scheme with digital descriptor modality.*** In addition to the log*P* and $\Delta Q_{CT}$ mentioned above, there are another 8 digital descriptors that are crucial in the prediction of $E_{form}$ (**Fig. 3**). The component descriptors include the size of the metal core ($N_{metal}$), the ratio of the number of doped metal atoms (*ratio*), and the differences between molar mass of the metals ($\Delta M$), respectively. Leveraging binary metallic phase diagrams as feature descriptors could capture the thermodynamics matching between two metals. $H_{mix}$ is selected as an easily accessible feature to describe the ability of miscibility between two metal elements. The interactions between two types of metal elements are elucidated by the differences between electronegativity ($\Delta\chi_M$), which is readily available parameters. In addition, some geometric descriptors, such as the average metal-metal distance (*D*) and the differences between atomic radius ($\Delta R$), are further selected for the formation energy prediction.

Coordination atoms in nanoclusters are usually sulfur (S) and phosphorus (P), while oxygen (O) atoms are commonly found in zeolites. The environmental electronegativity ($\chi_{env}$) can be used to represent the coordination interaction between the metal core and its surrounding environment, which can be expressed in equation (5).

$$\chi_{env} = \overline{\chi}_{metal} - \overline{\chi}_{sub} \quad (5)$$

where $\overline{\chi}_{metal}$ is the average electronegativity of the total atoms, and $\overline{\chi}_{sub}$ is the average electronegativity of the substrate, respectively. It is found that the values of $\Delta Q_{CT}$ for bimetallic nanoclusters and zeolites show the volcano-like correlation between the $\chi_{env}$, respectively, in **Fig. 3**. For bimetallic zeolites, the values of $\Delta Q_{CT}$ become larger with the values of $\chi_{env}$ more negative, indicating that larger electronegativity difference enhances the charge transfer by strengthening the interaction between metal atoms and O atoms around the channel. In contrast, bimetallic nanoclusters tend to exhibit larger $\Delta Q_{CT}$ values even with smaller electronegativity differences, likely due to their distinct coordination environments dominated by flexible organic ligands. The Pearson correlation coefficient matrix of these features is shown in **Fig. S4**, from which one can find that the top 3 important features are *ratio*, $\chi_{env}$, and $N_{metal}$, respectively. Shapley additive explanations (SHAP), derived from the concept of Shapley values in game theory, provide a fair attribution of contribution to each feature in the prediction process. In this framework, a feature's contribution is determined by averaging its marginal impact across all possible feature combinations, ensuring that the distribution of contributions is both fair and consistent. According to the SHAP analysis, the features of *ratio* and $\chi_{env}$ emerge as the most influential, which is consistent with the results obtained from the Pearson correlation coefficient matrix. The analysis indicates that medium-to-low values of *ratio* and higher values of $\chi_{env}$ are associated with more stable

structures. A larger electronegativity difference enhances the interaction between the metal core and its surrounding environment, ultimately leading to greater structural stability in bimetallic systems.

The random forest regression (RFR) model gives the good prediction of the formation energies based on the bimetallic nanocluster dataset among twelve models, as shown in **Fig. S5-S6**. To show the generalization performance of these features, the data of bimetallic zeolites are added to construct bimetallic nanocluster and zeolite dataset. The RFR model also keeps the good prediction performance, in which the MAE values of 0.18 eV/atom in **Fig. S7-S8** with the parameters listed in **Table S2**.

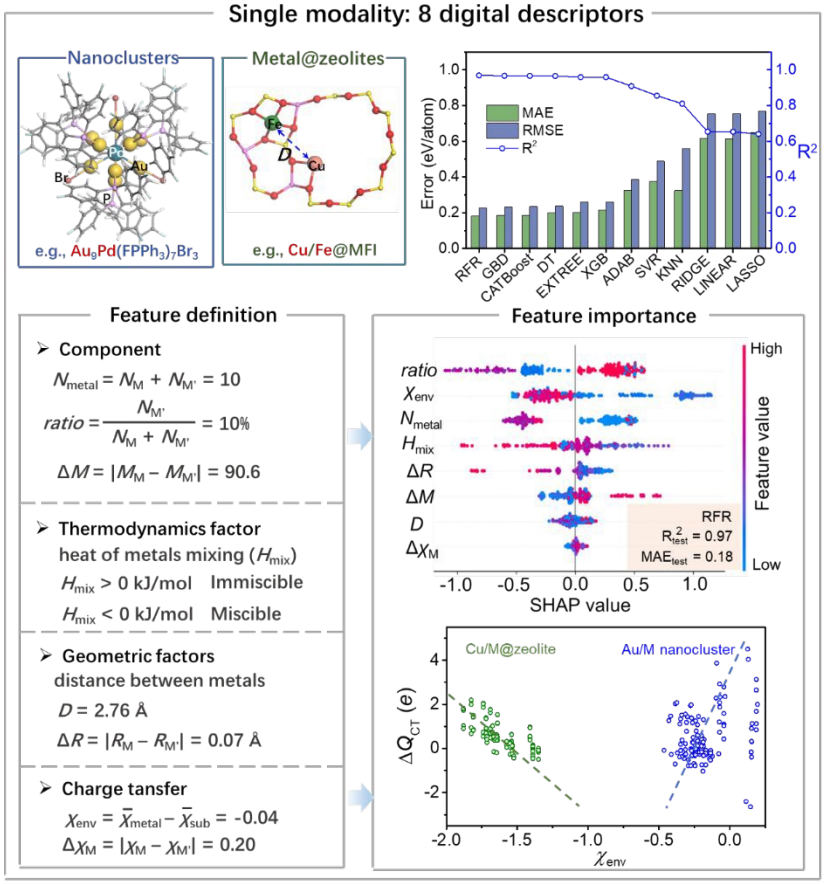


**Fig. 3** The 8-feature scheme model based on digital descriptor modality for the formation energy prediction.

However, the single data modality may be not entirely robust to underestimate the complicated interplay of these factors and may suffer from the overfitting limitation to give the reasonable prediction of the stability of the bimetallic materials. Graph-based models tend to lack interpretability, making it difficult to unravel the chemical factors behind predictions. On the other hand, models that rely solely on digital descriptors are prone to overfitting, primarily due to their inability to capture the full structural and environmental complexity of chemical systems. The multimodal machine learning (MML), a promising approach that integrates diverse data modalities, will be applied in the next subsection for prediction of formation energy.

***Formation energy prediction based on MML model.*** We have designed an MML model with contextual awareness, including graph (for metal core), SMILES (for ligand), and some digital descriptors (for physical properties), to predict the $E_{form}$ of the bimetallic nanoclusters in **Fig. 4**. The purpose of integrating multiple modalities, graph representations of the metal core, SMILES strings of the ligands, and digital descriptors such as mixing enthalpy ($H_{mix}$) and solubility (log$P$), is to capture complementary information about bimetallic nanoclusters that a single modality alone cannot fully represent. The graph modality encodes structural topology, SMILES provides chemical composition and ligand environment, and digital descriptors supply key thermodynamic and physicochemical properties. By combining these heterogeneous data streams in a shared latent space, the MML model could achieve contextual awareness and avoid the limitations of single-modality models, such as lack of interpretability or overfitting.

All the structures were collected into the nanocluster dataset to train the MML model, in which 8949 data (80%) were chosen as the training set, 1119 (10%) for the validation set, and the rest for the test set, as shown in **Table 1**. The framework of the MML model is illustrated in **Fig. 4a**. The bimetallic nanoclusters are initially separated into two parts: the core and the ligands. The metal core is represented by a molecular graph that captures its topological structure, $M_{core}$, which is subsequently encoded into graph embeddings. As mentioned above, the miscibility of two metals in the core could be reflected by $H_{mix}$ value, called $d_{Hmix}$. The chemical composition

View Article Online
DOI: 10.1039/D5SC04386C



of the ligands is represented using SMILES notation, $S_{ligands}$, which is encoded via MolT5[40], a pre-trained model for natural language text and molecule strings. The important feature of ligand solubility is described by digital values of log*P*, $d_{\log P}$. The log*P* values were taken from XLOGP3 [41] and our PoLogP [39], which gave similar performance in log*P* prediction. We encode these features using distinct encoders and project them into a shared latent space. The descriptor features are encoded by a single linear layer.

To encode the contextual information of the nanoclusters, we design a pre-fusion stage before the fusion stage. In the pre-fusion stage, the solubility properties of the ligands are added to the front and back ends of the core's graph features, and the enthalpy of mixing of the two metal elements is added to the front and back ends of the ligand SMILES features. The pre-fusion stage is designed to enhance the contextual awareness of the model by providing additional information about the ligands and the core. The augmented core and ligand features, along with the descriptor features, are then concatenated and fed into the fusion stage. Four layers of Mamba2 [42] are employed to facilitate the exchange of information between the multimodal features. The output of the fusion stage is pooled and passed into a regression head, which consists of linear layers and PReLU activation function units.

The model takes the core $M_{core}$, the ligands' SMILES strings $S_{ligands}$, and the descriptor features $D = [d_{\log P}, d_{Hmix}]$ as input. We denote the features decoded by the core encoder $\varphi_c$, the ligands encoder $\varphi_l$ , and the descriptor encoder $\varphi_d$ as $f_c$, $f_l$, and $f_d$, respectively.

In the pre-fusion stage, the core and ligands features are augmented as follows:

$$f_c^{aug} = \varphi_c([d_{\log P}, f_c, d_{\log P}]) \quad (6)$$

$$f_l^{aug} = \varphi_l([d_{Hmix}, f_l, d_{Hmix}]) \quad (7)$$

where $d_{\log P}$ and $d_{Hmix}$ are the descriptor features of solubility and enthalpy of mixing, respectively, and $\varphi_c$ and $\varphi_l$ are linear projection layers.

The augmented core and ligands features are concatenated with the descriptor features and fed into the fusion stage:

$$f_s = SSM([f_c^{aug}, f_l^{aug}, f_d]) \quad (8)$$

where SSM denotes the four continuous Mamba2 blocks and $f_s$ is the multimodal feature vector.

The output of the fusion stage is pooled and passed through the regression head to predict the formation energy of the bimetallic nanoclusters:

$$E_{form}^{MML} = \psi(\Theta(f_s)) \quad (9)$$

where Θ and $\psi$ are the pooling operation and the regression head, respectively.

The loss functions comprise the contrastive loss and the regression loss. To enable the model to learn the connection between the original nanoclusters and the unit of core and ligands, we employ the contrastive loss. The contrastive loss is calculated using the cross-entropy loss between the graph features of the original nanoclusters and the combination of the graph features of the core and the SMILES features of the ligands. The regression loss is calculated using the mean squared error between the predicted formation energy and the actual formation energy. The total loss is computed as the sum of the contrastive loss and the regression loss, with the details shown in Supporting Information.

MML could discover inherent relationships between the modalities, improving the predictive ability and generalization capability of models to surpass single-data-dimension limitations. Compared with the single-modal machine learning only with graph or numeric modality in **Table 1**, the smaller values of MAE in test set indicate the better performance of MML models. We investigate the impact of various descriptors on model performance further, as shown in **Fig.4b**. The MML model incorporating both log*P* and $H_{mix}$ achieves the best results, with an MAE of 0.055 eV/atom, RMSE of 0.209 eV/atom, and $R^2$ of 0.952. These results highlight the significance of contextual information from the nanoclusters for accurately predicting the formation energy of bimetallic nanoclusters. Additionally, we examine the individual contributions of solubility and the enthalpy of mixing. When either solubility or enthalpy of mixing is used as the sole descriptor, the model achieves MAEs of 0.072 eV/atom and 0.057 eV/atom, respectively. Both of these performances surpass the model without any descriptors, suggesting that ligand environment and miscibility of metal pairs are very important features in nanocluster design. As a result, the present MML model significantly improves prediction accuracy of formation energies, reaching lower mean absolute errors (0.055 eV/atom) in test set compared to graph-only or descriptor-only models, indicating good generalization to larger and experimentally synthesized nanoclusters.

The MML model enables rapid and reliable evaluation of large-sized nanoclusters containing hundreds to over a thousand atoms, which are computationally challenging for conventional DFT methods. The advantage of the constructed MML model is employed to realize the formation energies prediction for the large-sized structures. As shown in **Fig. 4d**, the selected bimetallic nanoclusters exhibit total atom counts ($N_{atom}$) ranging from 277 to 1317, which are much larger than those in training set. The predicted formation energies are all below -2.2 eV/atom, suggesting favorable thermodynamic stability consistent with experimental realizations. We also choose three nanoclusters, $Au_{23}Pd(CHT)_{17}$, $Au_{24}Cd(n BuS)_{18}$, and $Au_{24}Hg(n BuS)_{18}$, which are affordable in DFT calculations. The DFT formation energies are -3.56, -3.58, and -3.71 eV/atom, respectively, which are reproduced by MML prediction with MAE of 0.44 eV/atom. For example, a nanocluster in the external test set, $Au_{47}Cd_2(TBBT)_{31}$ ($N_{atom}$ = 793) [43], was predicted to have a formation energy of -3.34 eV/atom. Furthermore, a recently synthesized nanocluster, $Ag_{135}Cu_{60}(PET)_{60}Cl_{42}$ ($N_{atom}$ = 1317) [44], featuring a buckminsterfullerene-like silver kernel, was predicted to be thermodynamically stable with a formation energy of -2.28 eV/atom. This is in agreement with its successful one-pot synthesis via the reduction of a solution containing 4-$CH_3C_6H_4SO_3Ag$, $CuCl_2{\cdot}2H_2O$, and 2-phenylethanethiol in a mixed solvent system of dichloromethane and methanol using $NaBH_4$ as a reductant.

View Article Online
DOI: 10.1039/D5SC04386G





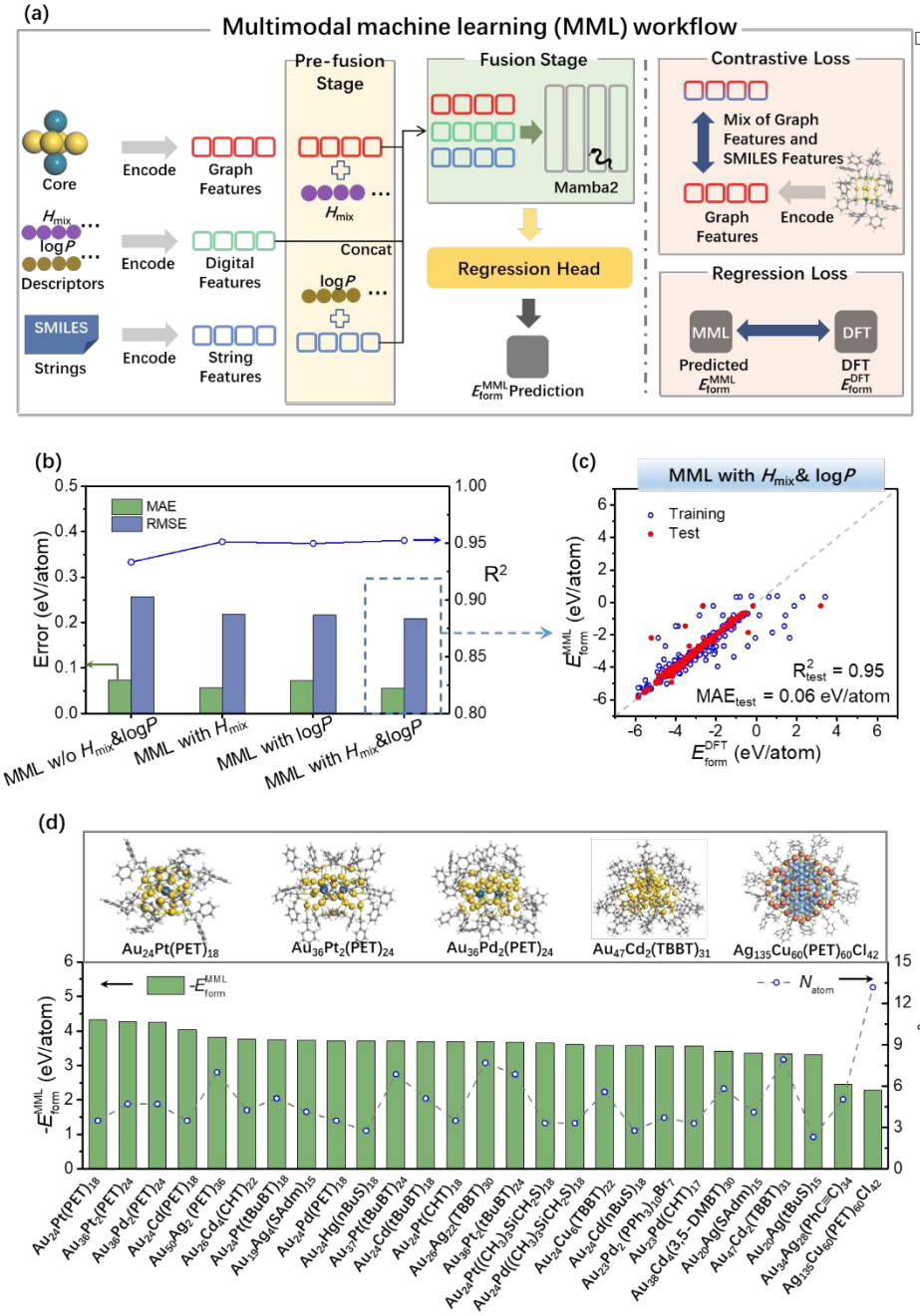


**Fig. 4** (a) The flowchart of formation energy prediction on bimetallic nanoclusters by multimodal machine learning. (b) comparison of the performance of the MML models; (c) prediction of formation energy ($E_{form}$) by the MML with log*P* and $H_{mix}$; (d) the prediction of the synthesized bimetallic nanoclusters.

**Accessibility prediction: accessibility index *v.s.* formation energy**

In order to provide useful information for guiding experimental synthesis, accessibility prediction was carried out with the consideration of geometric and electronic factors in bimetallic materials. Analogous to the concept of reduced mass of two-body system, the reduced atomic distance ($\tilde{D}$) is defined in equation (10),

$$\tilde{D} = 1 - \frac{c * \Delta R}{D + c * \Delta R} (10)$$

where $D$ represents the average interatomic distance between the two metals, $\Delta R$ denotes the difference in their atomic radii, and $c$ is an empirical scaling factor (set to 100) that ensures the $\Delta R$ term is appropriately weighted relative to $D$. When the size of two metals is similar, such as Au ($R$ = 144 Å) and Ag ($R$ = 144 Å) atoms in $Au_4Ag_2(PET)_8$, the values of $\Delta R$ is 0, leading to the $\tilde{D}$ of 1. While the average metal-metal distance (e.g., $D$ = 3.92 Å for Cu/Y@MOR) is much less than $c$*$\Delta R$, the values of $\tilde{D}$ may be close to 0. Our analysis indicates that the optimal reduced distances are typically around 0.3 for nanoclusters (e.g., $Au_4Ru_2(PET)_8(PPh_3)_2$, $Au_4Re_2(PET)_8(PPh_3)_2$, $Au_4Os_2(PET)_8(PPh_3)_2$) and 0.1 for zeolites (e.g., Cu/Sc@MOR,

Cu/Sc@MFI, Cu/Y@MFI), with the optimal metal-metal distances (*D*) of 3.5 Å for nanoclusters and 2.5 Å for zeolites, respectively.

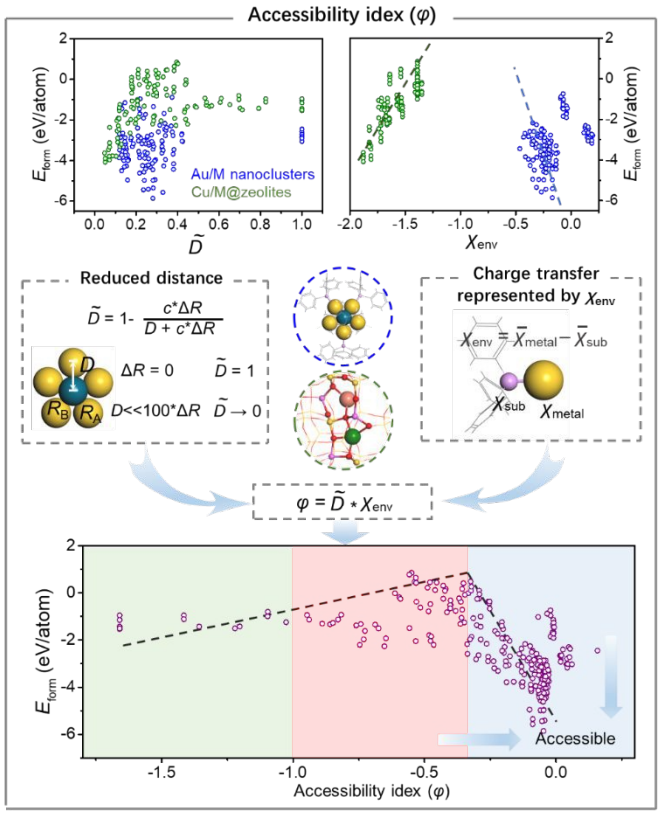


**Fig. 5** The definition of the terms of the accessibility index and their relationship with formation energy.

On the other hand, the electronegativity difference between the metal core and its coordination environment ($\chi_{env}$) serves as an effective indicator of charge transfer ($\Delta Q_{CT}$) between two metal atoms (**Fig. 3**). A volcano-like correlation between $\chi_{env}$ and stability is observed in **Fig. 5**, where the left and right branches correspond to Cu/M@zeolites and Au/M nanoclusters, respectively. Such a consistent trend drawn from different types of materials suggests that $\chi_{env}$ without relying on DFT calculations, could be used in the high-throughput screening of synthetically accessible bimetallic materials. Motivated by these observations, we propose a new descriptor, $\varphi$, to quantitatively evaluate the synthetic accessibility of bimetallic structures. The definition of $\varphi$ is presented as follows:

$$\varphi = \tilde{D} \cdot \chi_{env} \quad (11)$$

where $\tilde{D}$ is the reduced distance parameter that geometric difference, and $\chi_{env}$ captures the feature of charge transfer between two metals.

The most stable bimetallic structures are typically found within a characteristic energy basin where ϕ > -0.3 in **Fig. 5**. Thus, a larger $\varphi$ value indicates better geometric and electronic matching, both of which contribute to the enhanced stability and accessibility of the bimetallic materials.

The combined evaluation of $\varphi$ and $E_{form}$ can serve as a guideline for the efficient screening of bimetallic materials that are likely to be synthesizable. As shown in **Fig. 6a**, the relationship between the descriptors $H_{mix}$ and $\varphi$ with the $E_{form}$ reveals that, in general, bimetallic nanoclusters exhibit greater thermodynamic stability than metal-zeolite systems. The formation energies become more negative with the increasing trend of the $H_{mix}$ values for bimetallic nanoclusters, which can be attributed to the protection of the ligands in **Fig. 6b**. Ligands can cover the surface of bimetallic nanoclusters, reducing surface energy and passivating the 'active' low-coordinated metal atoms to enhance the thermodynamic stability. Some ligands (e.g., carbonyl, thiol) can form stable coordination environments to inhibit oxidation and other unfavorable chemical reactions by forming strong bonds with metal atoms, thereby preventing excessive aggregation or dissociation. Some dopped metals in bimetallic nanoclusters with higher values of $H_{mix}$ have been synthesized in experiment, *i.e.*, $[Au_{12}Ru(Ph_2PCH_2PPh_2)_6]^{2+}$ ($H_{mix}^{Au/Ru}$ = 15 kJ/mol), $[Au_{12}Ir(Ph_2PCH_2PPh_2)_6]^{3+}$ ($H_{mix}^{Au/Ir}$ = 13 kJ/mol), and $[Au_{12}Rh(Ph_2PCH_2PPh_2)_6]^{3+}$ ($H_{mix}^{Au/Rh}$ = 7 kJ/mol), respectively. [18] The seemingly immiscible bimetallic combination could be realized by using the strategy of the protected ligands. Gold nanoclusters containing immiscible metal pairs, specifically Au/Ru, Au/Re, and Au/Os, are identified as thermodynamically stable, with formation energies below -5 eV/atom in **Fig. 6c**. Representative examples include $Au_4Ru_2(PET)_8(PPh_3)_2$, $Au_4Re_2(PET)_8(PPh_3)_2$, $Au_4Os_2(PET)_8(PPh_3)_2$, all of which exhibit $\varphi$ values greater than -0.3, suggesting favorable synthetic accessibility. Among them, $Au_4Ru_2(PET)_8(PPh_3)_2$ has already been successfully synthesized and shown to enable light-driven $N_2$ fixation.[45] In contrast, bimetallic Cu/M@zeolites (where M = Ir, Re, Os) are predicted to be thermodynamically unstable, with corresponding $\varphi$ values of -0.53, -0.55, and -0.54, respectively, indicating that experimental synthesis of these Cu/M@zeolite structures may be challenging.

View Article Online
DOI: 10.1039/D5SC04386G

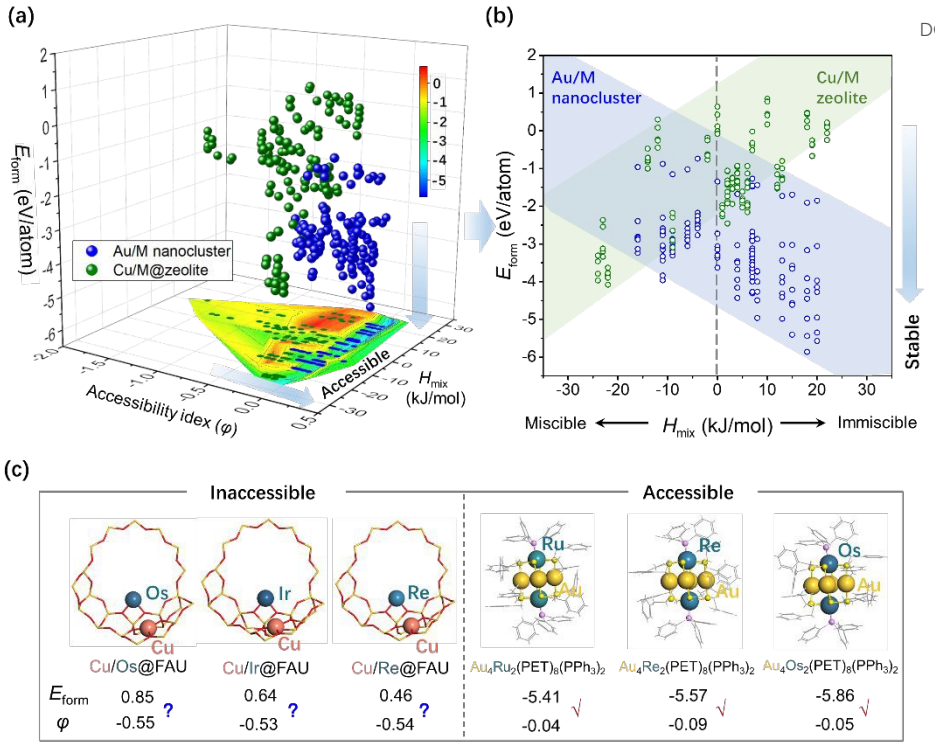


**Fig. 6** (a) The formation energy profile of bimetallic materials with $\varphi$ and $H_{mix}$; (b) the pairwise relationship between formation energy and $H_{mix}$; (c) the structures of inaccessible Cu/M@zeolites and accessible Au/M nanoclusters.

The training dataset, while primarily focused on ligand-protected nanoclusters and zeolites, contains a variety of metal combinations, stoichiometries, and coordination environments that capture essential patterns of metal-ligand interactions and stability. This diversity within the training data ensures that the model is not overfitted to a specific material type but rather learns generalizable features of bimetallic systems. The generalization of the proposed multimodal machine learning model beyond ligand-protected nanoclusters and zeolites originates from the intrinsic bimetallic pairing in the selected descriptors. The environmental electronegativity ($\chi_{env}$) describes the interaction between the metal core and its surrounding coordination environment, no matter whether it is in nanoclusters, zeolites, alloys, or 2D materials. Similarly, the mixing enthalpy ($H_{mix}$) reflects the miscibility between two metals, a property that is not restricted to a specific family but is applicable to all bimetallic systems. By incorporating such transferable descriptors that capture physicochemical principles, the model achieves predictive capability across different classes of bimetallic materials.

The machine learning model was further applied to 100 different materials, including metal-zeolites [28], nanoclusters [37], metal-loaded oxides/nitrides [32-34] at the interfaces, alloys [35-36], and 2D materials [29-31], spanning dimensionalities from three-dimensional to two-dimensional configurations. As summarized in **Table S4**, the synthesized configurations are predicted to exhibit thermodynamic stability under operational conditions. The stability index, $\varphi$, shows the correlation between the formation energies with Pearson correlation coefficient ($r$) of -0.63 in **Fig. 7**, indicating that a higher value of $\varphi$ may lead to a more stable structure. The predictive accuracy of model is expected to increase further by incorporating material-specific descriptors, which will enhance its ability to predict the stability of a broader range of bimetallic systems in future work.

View Article Online
DOI: 10.1039/D5SC04386G



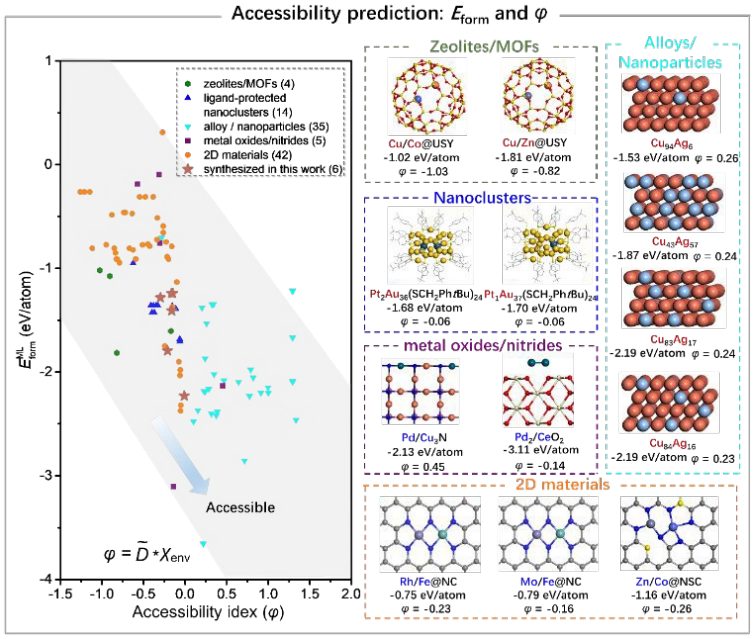


**Fig. 7** Accessibility prediction via $E_{form}$ and $\varphi$ for the external test set of bimetallic materials, including porous materials, nanoclusters, alloys, nanoparticles, metal oxides/nitrides, and 2D materials.

Bimetallic pairs of noble metals (Au/M, Pt/M) and non-noble metals (Cu/M, Ni/M) are predicted by the RFR algorithm, encompassing nanoclusters, metal-zeolites, 2D materials, *etc.*, as illustrated in **Fig. 8**, with associated standard deviation error bars. The color bar indicates the average values of stability index, $\varphi$, of these metal pairs. The stability of Au/M pairs seems to be higher than the Cu/M pairs, which can be attributed to the higher electronegativity ($\chi_{Au}$ = 2.54 *v.s.* $\chi_{Cu}$ = 1.90), allowing it to accept electrons when bonded with metals of lower electronegativity.

Among the noble metal pairs, the top three Au-based pairs identified are Au/Os, Au/Re, and Au/Ru with immiscible metal combinations, which are promising for future experimental realization. The formation energies for Au/Ag pairs are -2.59±0.22 eV/atom, suggesting the potential for experimental synthesis. By tuning the ligand environment, $PPh_3$, $(CF_3)_2PhC{\equiv}CH$, and $Cl^-$ were selected to protected the cores to form the Au/Ag nanoclusters in the following section, with the $\varphi$ in the range of -0.16 ~ -0.10. Due to the high cost and scarcity of noble metals, introducing non-noble metals into noble metal systems to form bimetallic pairs is essential to achieve a balance between performance and cost. For non-noble metals, $d^1$ (Y, Sc), $d^2$ (Ti, Zr), and $d^{10}$ (Au, Cd, Zn) metals are predicted to exhibit more stable structures with Cu/M pairs. And Ni element is favorable to form the metal pairs with $d^{10}$ metals (Au, Ag).

Another three miscible/immiscible bimetallic pairs, Ni/Pt, Cu/Gd, and Au/Ni, exhibit formation energies lower than -1 eV/atom according to the wind rose diagrams, indicating their thermodynamic stability. The nitrogen-doped carbon surface provides a favorable support for anchoring these metal species. The corresponding $\varphi$ values for Ni/Pt@NC, Cu/Gd@NC, and Au/Ni@NC are calculated to be -0.30, -0.21, and -0.16, respectively, suggesting that these structures are experimentally accessible. Taking the multifactors of $E_{form}$, $\varphi$, and $H_{mix}$ into account, these systems are selected in the following section to validate the applicability and predictive power of the constructed machine learning model.

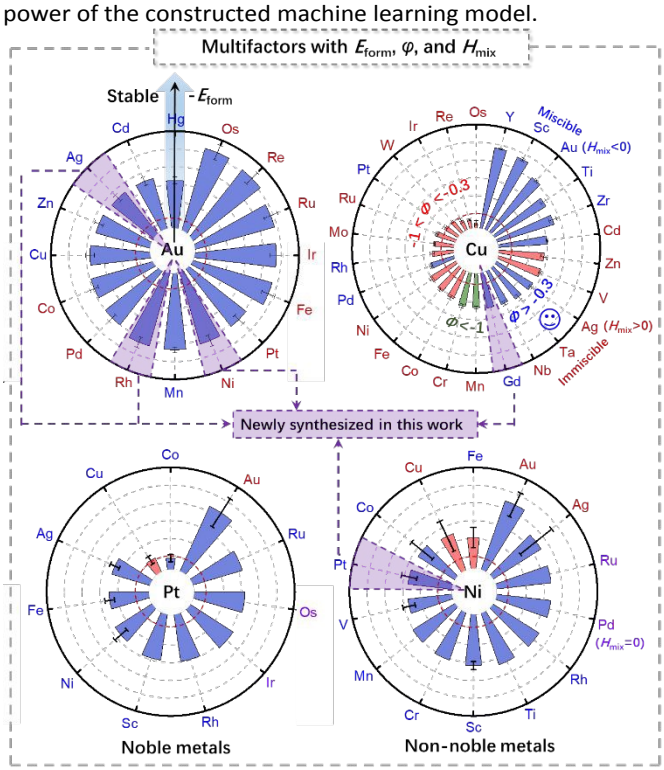


**Fig. 8** The accessibility prediction via $E_{form}$, $\varphi$, and $H_{mix}$ for the bimetallic pairs comprising noble metals (Au/M, Pt/M) and base metals (Cu/M, Ni/M) predicted by the machine learning.

View Article Online
DOI: 10.1039/D5SC04788C



**Newly synthesized bimetallic materials as accessibility tests**

Among the vast combinations of metal pairs, the prediction of accessibility could accelerate the design and discovery of promising bimetallic candidates. Two nanocluster crystals are successfully synthesized in experiment in **Fig. S9-S11** (for experiment details, see Supporting Information). The structures of $Au_{36}Ag_{38}((CF_3)_2PhC{\equiv}C)_{30}Cl_{10}$ (short for $Au_{36}Ag_{38}$) and $Au_{38}Ag_{33}((CF_3)_2PhC{\equiv}C)_{30}Cl_8$ (short for $Au_{38}Ag_{33}$) are solved by single-crystal X-ray diffraction in **Fig. 9**. $Au_{36}Ag_{38}$ can be viewed as a core–shell structure with the predicted formation energy of -1.24 eV/atom. The $Au_{21}Ag_3$ core is enclosed by an $Ag_{35}$ shell coordinated with 10 $Cl^-$ ligand, and the outermost layer consist of 15 monomeric RC≡C–Au–C≡CR staples. $Au_{38}Ag_{33}$, with the same formation energy of -1.24 eV/atom, shares a similar structure and ligand arrangement, and co-crystallized with $Au_{36}Ag_{38}$, which made it difficult to separate the single crystals of the two products via crystallization. Like $Au_{36}Ag_{38}$, $Au_{38}Ag_{33}$ is also stabilized by 15 monomeric RC≡C–Au–C≡CR staples. In addition to the surface staple structure, $Au_{38}Ag_{33}$ contains an $Au_{23}$ core and an $Ag_{33}$ shell coordinated with 8 $Cl^-$ ligand. Interestingly, the constructed ML model can be further to predict the formation energy of trimetallic nanocluster. As shown in **Fig. 9b**, $Au_9AgRh(PPh_3)_8Cl_2$ (denoted as $Au_9AgRh$) was obtained by doping Ag and Rh on the basis of $[Au_{11}(PPh_3)_8Cl_2]^-$, with a formation energy of -2.23 eV/atom. It has a similar structure to $Au_{11}$, but the doping of Ag and Rh causes a slight distortion in its structure. The two positions coordinated with $Cl^-$ ligand are co-occupied by Au/Ag/Rh.

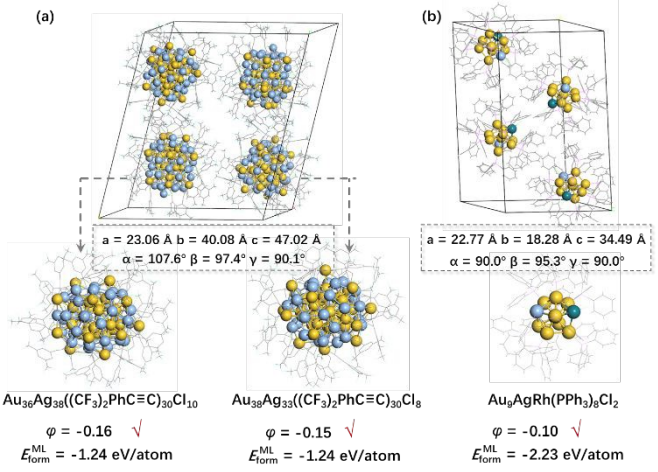


**Fig. 9** The crystal structures and ML predicted formation energies, $E_{form}^{ML}$, of (a) $Au_{36}Ag_{38}((CF_3)_2PhC{\equiv}C)_{30}Cl_{10}$ and $Au_{38}Ag_{33}((CF_3)_2PhC{\equiv}C)_{30}Cl_8$ and (b) $Au_9AgRh(PPh_3)_8Cl_2$.

Three bimetallic pairs supported on nitrogen-doped carbon (NC) were predicted to be stable with $E_{form}^{ML}$ of -1.79, -1.41, and -1.28 eV/atom for Au/Ni@NC, Cu/Gd@NC, and Ni/Pt@NC systems, respectively, in **Fig. 10a**. The DFT-calculated formation energies were -2.45, -1.81, and -1.75 eV/atom for these systems, demonstrating qualitative alignment with the predicted stability trend. The projected density of states (PDOS) also reveals a interaction between the *d* orbitals of bimetallic centers (Au, Ni) and the orbitals of the coordination N atoms near the Fermi level. The charge transfer between the bimetallic centers and surrounding N atoms could strengthen the stability of the Au/Ni@NC.

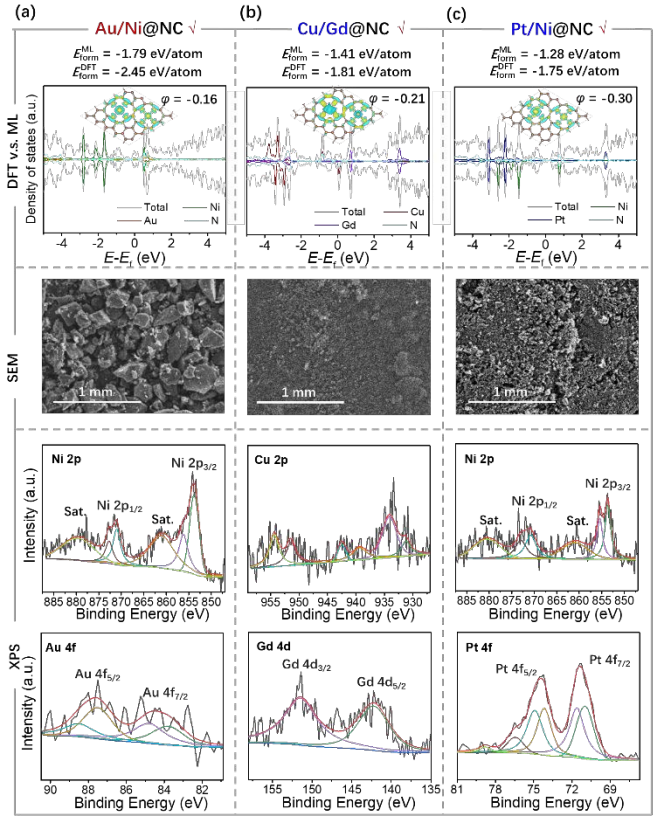


**Fig. 10** DFT and the ML predicted formation energies and density of states and charge density differences, the SEM images, and XPS spectra of (a) Au/Ni@NC, (b) Cu/Gd@NC, and (c) Ni/Pt@NC, respectively.

The Au/Ni@NC, Cu/Gd@NC, and Ni/Pt@NC materials were synthesized in experiment with the image of scanning electron microscope (SEM) shown in **Fig. 10b**, (for experimental details, see Supporting Information). Powder X-ray diffraction (XRD) provided crystal structure information at the macroscale in **Fig. S12**. The structures of Au/Ni@NC, Cu/Gd@NC, and Ni/Pt@NC were further characterized by X-ray Photoelectron Spectroscopy (XPS), which could reveal the bimetallic chemical composition and surface chemical state in **Fig. 10c** and **Fig. S13-S15**. For Au/Ni@NC, a typical Ni $2p_{3/2}$ and $2p_{1/2}$ doublet accompanied by two satellite peaks indicated the positive oxidation state of Ni atoms in Au/Ni@NC. [46] The XPS peaks of Au *4f* were characterized by two sets of doublets, the peaks located at 87.50 and 83.80 eV correspond to Au $4f_{7/2}$ and Au $4f_{5/2}$ of Au(0). The peaks at 88.50 and 84.80 eV could be attributed to the Au( Ⅲ ) species. [47] For Cu/Gd@NC, two characteristic peaks could be attributed to Cu(0) species at 931.20 eV and 951.42 eV, and the other two peaks at 934.12 eV and 954.36 eV were assigned to Cu(II) species. [48] Two peaks appear at 151.44 and 142.20 eV, which were attributed to Gd $4d_{3/2}$ and Gd $4d_{5/2}$, indicating the existence of the Gd element in synthesized material. [49] As reflected by XPS results of Pt *4f* in Ni/Pt@NC, the spectra were deconvoluted into two spin-orbit

doublets, indicating the existence of the Pt element in synthesized material. [50] These results demonstrate that the ML-predicted formation energies are qualitatively consistent with DFT calculations and experimental observations, indicating the capability to design the stable bimetallic materials.

## Conclusions

In this study, we have presented the MML model and accessibility index to identify stable bimetallic materials that can be experimentally synthesized. By integrating the molecule graph of the metal core and the SMILES notation of the ligand with the addition of $H_{mix}$ and log*P*, MML model could predict the stability of the bimetallic nanoclusters with up to thousands of atoms. The stability of bimetallic materials could be further adjusted by the coordination environment, in which the protected ligands prevented the aggregation or dissociation of the metal cores. The accessibility index based on the combination of geometric and electronic factors has been successfully extended to external test sets for experimentally obtained bimetallic materials, including the metal-zeolites, nanoclusters, alloys, metal oxides/nitrides, and 2D materials. When the $\varphi$ is greater than -0.3, the corresponding bimetallic material is considered potentially synthesizable in experiment. Notably, our machine learning model has effectively guided the synthesis of six new structures, including nanoclusters and 2D materials, which were anticipated to exhibit stability. The proposed machine learning approach holds significant promise for the discovery and synthesis of bimetallic materials in experimental settings.

## Conflicts of interest

There are no conflicts to declare.

## Acknowledgements

This work was supported by the National Key Research and Development Program of China (2023ZD0120700), the National Natural Science Foundation of China (grant no.22033004, 22373049, 62222604, 62192783, 22125202, and 92461312), the Natural Science Foundation of Jiangsu Province (BK20232012), and the Jiangsu Funding Program for Excellent Postdoctoral Talent (grant no. 2023ZB655). We are grateful to the High Performance Computing Centre of Nanjing University for providing the IBM Blade cluster system.

## Author contributions

Jing Ma and Yuming Gu initiated the project. Yuming Gu carried out the DFT calculations and built the GCNN model and 8-feature scheme model. Yating Gu, Jiawei Chen, Xinyi Liang, Dong Zheng, and Fengqi Song constructed the datasets. Shisi Tang and Yan Zhu performed the synthesis of new nanoclusters. Maochen Yang, Zekun Li, Yang Gao, and Yinghuan Shi designed the multimodal machine learning frameworks. All authors contributed to the discussion of the results as well as the writing and revision of the manuscript.

View Article Online DOI: 10.1039/D5SC04386G

## Notes and references

1 X. Liu, X. Cai, Y. Zhu. *Acc. Chem. Res.* **2023,** *56* (12), 1528-1538.
2 L. Liu, A. Corma. *Chem. Rev.* **2023,** *123* (8), 4855-4933.
3 C. Yang, B. H. Ko, S. Hwang, Z. Liu, Y. Yao, W. Luc, M. Cui, A. S. Malkani, T. Li, X. Wang, J. Dai, B. Xu, G. Wang, D. Su, F. Jiao, L. Hu. *Science Advances* **2020,** *6*, eaaz6844.
4 L. Zhang, Z. Xie, J. Gong. *Chem. Soc. Rev.* **2016,** *45* (14), 3916-3934.
5 K. D. Gilroy, A. Ruditskiy, H.-C. Peng, D. Qin, Y. Xia. *Chem. Rev.* **2016,** *116* (18), 10414-10472.
6 J. L. Durham, A. S. Poyraz, E. S. Takeuchi, A. C. Marschilok, K. J. Takeuchi. *Acc. Chem. Res.* **2016,** *49* (9), 1864-1872.
7 K. Kusada, M. Yamauchi, H. Kobayashi, H. Kitagawa, Y. Kubota. *J. Am. Chem. Soc.* **2010,** *132*, 15896-15898.
8 C. Srivastava, S. Chithra, K. D. Malviya, S. K. Sinha, K. Chattopadhyay. *Acta Mater.* **2011,** *59* (16), 6501-6509.
9 Q. Zhang, K. Kusada, D. Wu, T. Yamamoto, T. Toriyama, S. Matsumura, S. Kawaguchi, Y. Kubota, H. Kitagawa. *Nat. Commun.* **2018,** *9* (1), 510.
10 K. Kusada, T. Yamamoto, T. Toriyama, S. Matsumura, K. Sato, K. Nagaoka, K. Terada, Y. Ikeda, Y. Hirai, H. Kitagawa. *J. Phys. Chem. C* **2020,** *125* (1), 458-463.
11 M. Meischein, A. Garzón-Manjón, T. Hammerschmidt, B. Xiao, S. Zhang, L. Abdellaoui, C. Scheu, A. Ludwig. *Nanoscale Advances* **2022,** *4* (18), 3855-3869.
12 B. B. Rajeeva, P. Kunal, P. S. Kollipara, P. V. Acharya, M. Joe, M. S. Ide, K. Jarvis, Y. Liu, V. Bahadur, S. M. Humphrey, Y. Zheng. *Matter* **2019,** *1* (6), 1606-1617.
13 J. Feng, D. Chen, P. V. Pikhitsa, Y.-h. Jung, J. Yang, M. Choi. *Matter* **2020,** *3* (5), 1646-1663.
14 P.-C. Chen, M. Gao, C. A. McCandler, C. Song, J.Jin, Y. Yang, A. L. Maulana, K. A. Persson, P. Yang. *Nat. Nanotechnol.* **2024,** *19*, 775-781.
15 S. Yang, S. Chen, L. Xiong, C. Liu, H. Yu, S .Wang, N. L. Rosi, Y. Pei, M. Zhu. *J. Am. Chem. Soc.* **2018,** *140* (35), 10988-10994.
16 C. Zhou, H. Li, Y. Song, F. Ke, W. W. Xu, M. Zhu. *Nanoscale* **2019,** *11* (41), 19393-19397.
17 C. Yao, N. Guo, S. Xi, C.-Q. Xu, W. Liu, X. Zhao, J. Li, H. Fang, J. Su, Z. Chen, H. Yan, Z. Qiu, P. Lyu, C. Chen, H. Xu, X. Peng, X. Li, B. Liu, C. Su, S. J. Pennycook, C.-J. Sun, J. Li, C. Zhang, Y. Du, J. Lu. *Nat. Commun.* **2020,** *11* (1), 4389.
18 S. Takano, H. Hirai, T. Nakashima, T. Iwasa, T. Taketsugu, T. Tsukuda. *J. Am. Chem. Soc.* **2021,** *143* (28), 10560-10564.
19 Y. Gu, S. Tang, X. Liu, X. Liang, Q. Zhu, H. Wu, X. Yang, W. Jin, H. Chen, C. Liu, Y. Zhu, J. Ma. *J. Mater. Chem. A* **2024,** *12* (8), 4460-4472.
20 J. Jang, G. H. Gu, J. Noh, J. Kim, Y. Jung. *J. Am. Chem. Soc.* **2020,** *142* (44), 18836-18843.
21 A. Ghosh, S. Datta, T. Saha-Dasgupta. *J. Phys. Chem. C* **2022,** *126* (15), 6847-6853.
22 J. Ock, S. Badrinarayanan, R. Magar, A. Antony. *Nature Machine Intelligence* **2024,** *6* (12), 1501-1511.
23 N. Jeong, S. Park, S. Mahajan, J. Zhou, J. Blotevogel, Y. Li, T. Tong, Y. Chen. *Nat. Commun.* **2024,** *15* (1), 10918.
24 S. Wang, S. Gong, T. Böger, J. A. Newnham, D. Vivona, M. Sokseiha, K. Gordiz, A. Aggarwal, T. Zhu, W. G. Zeier, J. C. Grossman, Y. Shao-Horn. *Chem. Mater.* **2024,** *36* (23), 11541-11550.
25 X. Yan, A. Sedykh, W. Wang, B. Yan, H. Zhu. *Nat. Commun.* **2020,** *11*, 2519.
26 X. Yan, A. Sedykh, W. Wang, X. Zhao, B. Yan, H. Zhu. *Nanoscale* **2019,** *11*, 8352-8362.

View Article Online
DOI: 10.1039/D5SC04386G



27 W. Wang, X. Yan, L. Zhao, D. P. Russo, S. Wang, Y. Liu, A. Sedykh, X. Zhao, B. Yan, H. Zhu. *J. Cheminformatics* **2019,** *11*, 6.
28 T. Chen, W. Yu, C. K. T. Wun, T.-S. Wu, M. Sun, S. J. Day, Z. Li, B. Yuan, Y. Wang, M. Li, Z. Wang, Y.-K. Peng, W.-Y. Yu, K.-Y. Wong, B. Huang, T. Liang, T. W. B. Lo. *J. Am. Chem. Soc.* **2023,** *145* (15), 8464-8473.
29 J. Hao, H. Zhu, Q. Zhao, J. Hao, S. Lu, X. Wang, F. Duan, M. Du. *Nano Research* **2023,** *16* (7), 8863-8870.
30 Z. Li, S. Ji, C. Wang, H. Liu, L. Leng, L.Du, J. Gao, M. Qiao, J. H. Horton, Y. Wang. *Adv. Mater.* **2023,** *35* (25), 2300905.
31 L. Zhang, J. Feng, S.Liu, X. Tan, L. Wu, S. Jia, L. Xu, X. Ma, X. Song, J. Ma, X. Sun, B.Han. *Adv. Mater.* **2023,** *35* (13), 2209590.
32 J. Fu, J. Dong, R. Si, K. Sun, J. Zhang, M. Li, N.Yu, B. Zhang, M. G. Humphrey, Q. Fu, J. Huang. *ACS Catalysis* **2021,** *11* (4), 1952-1961.
33 Y. Lou, F. Jiang, W. Zhu, L. Wang, T. Yao, S. Wang, B. Yang, B. Yang, Y. Zhu, X. Liu. *Applied Catalysis B: Environmental* **2021,** *291*, 120122.
34 Z. Zhang, S.Chen, J.Zhu, C. Ye, Y. Mao, B. Wang, G. Zhou, L. Mai, Z. Wang, X. Liu, D. Wang. *Nano Lett.* **2023,** *23* (6), 2312-2320.
35 K. Qi, Y. Zhang, N. Onofrio, E. Petit, X. Cui, J. Ma, J. Fan, H. Wu, W. Wang, J. Li, J. Liu, Y.Zhang, Y. Wang, G. Jia, J.Wu, L. Lajaunie, C. Salameh, D. Voiry. *Nature Catalysis* **2023,** *6* (4), 319-331.
36 D. Wei, Y. Wang, C.-L. Dong, Z. Zhang, X. Wang, Y.-C. Huang, Y. Shi, X. Zhao, J. Wang, R. Long, Y. Xiong, F. Dong, M. Li, S. Shen *Angew. Chem. Int. Ed.* **2023,** *62*, e202217369.
37 X. Liu, E.Wang, M. Zhou, Y. Wan, Y. Zhang, H. Liu, Y. Zhao, J. Li, Y. Gao, Y. Zhu. *Angew. Chem. Int. Ed.* **2022,** *61*, e202207685.
38 Z. Liu, L. Lin, Q. Jia, Z. Cheng, Y. Jiang, Y. Guo, J. Ma. *J. Chem. Inf. Model.* **2021,** *61* (3), 1066-1082.
39 Q. Jia, Y. Ni, Z. Liu, X. Gu, Z. Cui, M. Fan, Q. Zhu, Y. Wang, J. Ma. *J. Chem. Inf. Model.* **2022,** *62* (20), 4928-4936.
40 C. Edwards, T. Lai, K. Ros, G. Honke, K. Cho, H. Ji. *arXiv preprint arXiv:2204.11817* **2022**.
41 T. Cheng, Y. Zhao, X. Li; F. Lin;, Y. Xu, X. Zhang, Y. Li, R. Wang, L. Lai. *J. Chem. Inf. Model.* **2007,** *47* (6), 2140-2148.
42 T. Dao, A. Gu. *arXiv preprint arXiv:2405.21060* **2024**.
43 S. Zhuang, D. Chen, L. Liao, Y. Zhao, N. Xia, W. Zhang, C. Wang, J. Yang, Z. Wu. *Angew. Chem. Int. Ed.* **2020,** *59*, 3073-3077.
44 L. Tang, W. Dong, Q.Han, B. Wang, Z. Wu, S. Wang. *Nature Synthesis* **2025**, 10.1038/s44160-024-00723-1.
45 Y. Sun, W. Pei, M. Xie, S. Xu, S. Zhou, J. Zhao, K. Xiao, Y. Zhu. *Chem. Sci.* **2020,** *11* (9), 2440-2447.
46 X. Zhang, H. Su, P. Cui, Y.Cao, Z. Teng, Q. Zhang, Y. Wang, Y. Feng, R. Feng, J. Hou, X. Zhou, P. Ma, H. Hu, K. Wang, C. Wang, L. Gan, Y. Zhao, Q. Liu, T. Zhang, K. Zheng. *Nat. Commun.* **2023,** *14* (1), 7115.
47 J. Zhao, H. Wang, H. Geng, Q. Yang, Y. Tong, W. He. *ACS Applied Nano Materials* **2021,** *4* (7), 7253-7263.
48 X .Zhou, M. Wang, J. Chen, X. Su. *Talanta* **2022,** *245*, 123451.
49 S. Ning, M. Li, X. Wang, D. Zhang, B. Zhang, C. Wang, D. Sun, Y. Tang, H. Li, K. Sun, G. Fu. *Angew. Chem. Int. Ed.* **2023,** *62*, e202314565.
50 F. Zhou, X. Ke, Y. Chen, M. Zhao, Y. Yang, Y. Dong, C. Zou, X.-A. Chen, H. Jin, L. Zhang, S. Wang. *Journal of Energy Chemistry* **2024,** *88*, 513-520.

View Article Online
DOI: 10.1039/D5SC04386G

The data are available from the corresponding author on reasonable request.